CrossMark

Serendipitous Archival Observations of a New Ultradistant Comet C/2019 E3 (ATLAS)

Man-To Hui (許文韜)[1] , Robert Weryk[2] , Marco Micheli[3] , Zhong Huang (黃中)[1], and Richard Wainscoat[4]

[1] State Key Laboratory of Lunar and Planetary Science, Macau University of Science and Technology, Avenida Wai Long, Taipa, Macau; mthui@must.edu.mo, manto@hawaii.edu
[2] Physics and Astronomy, The University of Western Ontario, 1151 Richmond Street, London, ON N6A 3K7, Canada
[3] ESA NEO Coordination Centre, Planetary Defence Office, Largo Galileo Galilei 1, I-00044 Frascati (RM), Italy
[4] Institute for Astronomy, University of Hawai'i, 2680 Woodlawn Drive, Honolulu, HI 96822, USA

Abstract

We identified a new ultradistant comet C/2019 E3 (ATLAS) exhibiting preperihelion cometary activity at heliocentric distances $\gtrsim 20$ au, making it the fourth member of this population after C/2010 U3 (Boattini), C/2014 UN_{271} (Bernardinelli–Bernstein), and C/2017 K2 (PANSTARRS). From serendipitous archival data, we conducted analyses of the comet, finding that the activity was consistent with steady-state behavior, suggestive of sublimation of supervolatiles; that the cross section of dust increased gradually on the inbound leg of the orbit, varying with heliocentric distances as $r_{H}^{-1.5 \pm 0.4}$; and that the dust was produced at a rate of $\gtrsim 10^2 \, \mathrm{kg \, s^{-1}}$ within the observed timespan. Our modeling of the largely symmetric morphology of the comet suggests that the dust environment was likely dominated by mm-scale dust grains ejected at speeds $\lesssim 0.4 \, \mathrm{m \, s^{-1}}$ from the sunlit hemisphere of the nucleus. Assuming a typical geometric albedo of 0.05 and adopting several simplistic thermophysical models, we estimated the nucleus to be at least ~ 3 km across. We also measured the color of the comet to be consistent with other long-period comets, except being slightly bluer in $g - r$. With our astrometric measurements, we determined an improved orbit of the comet, based upon which we derived that the comet is dynamically new and that its perihelion distance will further shrink due to the Galactic tide. We conclude the paper by comparing the known characteristics of the known ultradistant comets.

Unified Astronomy Thesaurus concepts: Long period comets (933); Comets (280); Oort cloud objects (1158)

1. Introduction

Recent years have witnessed a burst of interest in research on ultradistant comets, thanks to discoveries of three such objects, C/2017 K2 (PANSTARRS), C/2010 U3 (Boattini), and C/2014 UN_{271} (Bernardinelli–Bernstein), which exhibited activity in unprecedented observations of preperihelion heliocentric distances $r_{H} \gtrsim 20$ au (Jewitt et al. 2017; Meech et al. 2017; Hui et al. 2018, 2019; Bernardinelli et al. 2021). Deeply frozen for the majority of their lifetime, these comets are conceived to be the most primitive small bodies in the Solar System bearing significant scientific importance. Largely limited by the number of available samples, very little is known about how these comets are active at such large distances from the Sun. The current overall understanding is that cometary activity at $r_{H} \gtrsim 20$ au preperihelion is most likely driven by sublimation of supervolatiles such as CO and CO_2, which are reported to be abundant in comets (e.g., A'Hearn et al. 2012). At such great distances from the Sun, the equilibrium surface temperature is $\lesssim 60$ K, which may be too low even for crystallization of amorphous water ice (e.g., Guilbert-Lepoutre 2012). Interestingly, some recent models predicted that even comets in the Oort cloud have been intensively processed by cosmic-ray bombardment, thereby depleting CO (but not CO_2 or CH_4) in the outermost ~ 10 m of these cometary nuclei (Gronoff et al. 2020; Maggiolo et al. 2020). This appears to be supported by the measured production rates of CO and CO_2 of dynamically new comets, whose activity tends to be dominated by CO_2

rather than CO (Harrington Pinto et al. 2022). In addition, observations of active ultradistant comets pose a serious challenge to the classical comet model, which predicts no activity whatsoever for comets at these heliocentric distances, because drag forces from sublimating supervolatiles are not supposed to be strong enough to overcome interparticle cohesion (Jewitt et al. 2019). In order to understand better how ultradistant comets as well as comets in general are active, we feel the necessity to search for more comets of this kind in order to increase the available sample size.

In this paper, we report on the fourth ultradistant comet that exhibited preperihelion cometary activity at $r_{H} \gtrsim 20$ au, C/2019 E3 (ATLAS), using serendipitous prediscovery archival data. As the name suggests, the long-period comet was discovered by the Asteroid Terrestrial-impact Last Alert System (ATLAS) survey, on UTC 2019 March 5 at $r_{H} = 13.6$ au (Young et al. 2019). The latest orbital solution by JPL Horizons shows that the current osculating heliocentric orbit of the comet is slightly hyperbolic (eccentricity $e = 1.002$) and highly inclined to the ecliptic plane (orbital inclination $i = 84°.3$), and that it recently reached its perihelion at $q = 10.3$ au in 2023 mid-November.[5] In this paper, we first detail the serendipitous archival observations of the comet in Section 2, present results in Section 3, then discuss our analyses in Section 4, and finally summarize in Section 5.

2. Observations

We primarily used the Solar System Object Image Search (SSOIS) tool (Gwyn et al. 2012) at the Canadian Astronomy

---

[5] See the solution by JPL Horizons at https://ssd.jpl.nasa.gov/tools/sbdb_lookup.html#/?sstr=2019e3.
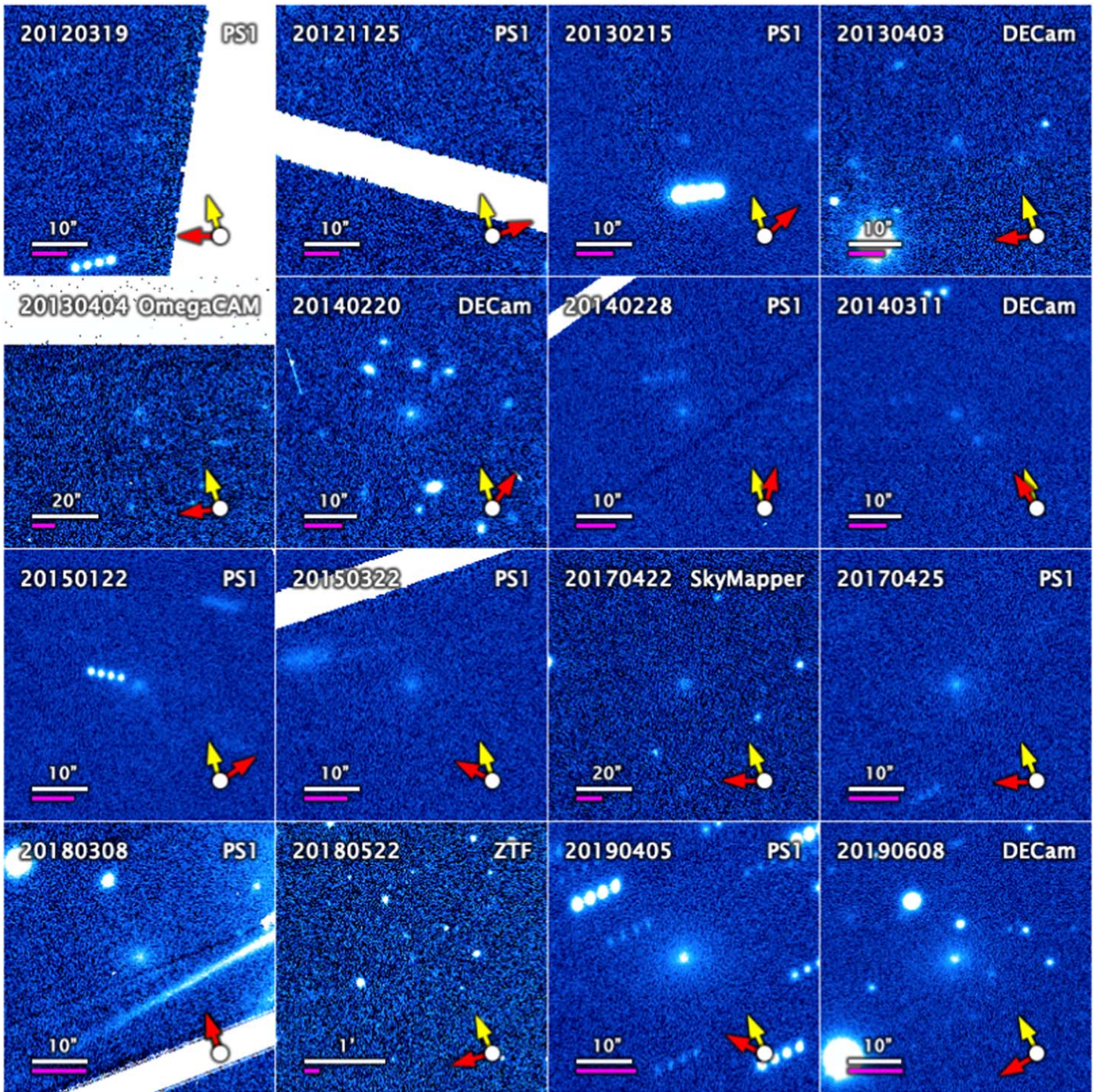
Figure 1. Collage of selected serendipitous archival observations of C/2019 E3, displayed in logarithmic scale at preperihelion heliocentric distances from ∼23 to 13 au. The comet is placed at the center of each panel. White stripes in some of the panels are CCD chip/cell gaps. Position angles of the antisolar direction and the negative heliocentric velocity projected in the sky plane are marked by the red and yellow arrows, respectively. Also shown are two scale bars, one with apparent lengths labeled, and the other one in magenta representing a linear length of 10^5 km projected at the observer-centric distance of the comet. J2000 equatorial north points upward and east to the left.

Data Centre (CADC) to search for prediscovery serendipitous observations of C/2019 E3. In general, we were able to detect the comet in archival images from five different telescopes, Blanco 4 m, Pan-STARRS 1 (PS1), SkyMapper, VLT Survey Telescope (VST), and the Zwicky Transient Facility (ZTF), all the way back to 2012. Selected archival images of the comet are shown in Figure 1. In the following, we detail these observations separately based on the used telescopes.

2.1. Víctor M. Blanco 4 m Telescope

Serendipitous archival observations of the comet in the g, i, and z filters from the Dark Energy Camera (DECam; Flaugher et al. 2015) on the Víctor M. Blanco 4 m telescope at Cerro Tololo Inter-American Observatory, Chile were identified. The camera houses 62 2k × 4k CCD chips at the prime focus, covering a hexagon-shaped 2°.2 diameter field of view (FOV) with an image scale of 0″.26 pixel^{-1}. The comet was located

almost exactly at the ephemeris positions returned by JPL Horizons in the prediscovery archival DECam data on four different nights, plus one in 2019 somewhat over a year after the comet had been discovered (see Table 1). We estimated seeing by measuring the FWHM of field stars to be $1\overset{''}{.}0$–$1\overset{''}{.}3$.

2.2. Pan-STARRS

Archival data from the two 1.8 m Pan-STARRS survey telescopes (Chambers 2016) on the summit of Haleakala, Maui, USA, including *w*-band images not publicly available, were searched based on ephemeris comparisons with the metadata of each image. These telescopes have large $3\overset{\circ}{.}1$ FOVs with a grid of 60 CCD chips, each further divided into 8×8 arrays of 590×598 pixel CCD cells having a $0\overset{''}{.}25$ pixel scale. Only PS1 observed the comet, in *w*-, *r*-, *i*-, and *z*-band images from 2012 to 2019, each of which has been astrometrically and photometrically calibrated (Waters et al. 2020). The FWHM of background stars varied between $0\overset{''}{.}9$ and $1\overset{''}{.}6$.

2.3. SkyMapper

Located at Siding Spring Observatory, Australia, SkyMapper is a 1.3 m survey telescope attached to a camera mosaicked by 32 CCD chips, each having 2048×4096 pixels at an image scale of $0\overset{''}{.}50$ pixel^{-1}, at the focal plane (Keller et al. 2007). The serendipitous two-night multiband observations of C/2019 E3 from 2017 April returned by SSOIS were conveniently cropped to a dimension of $\sim 10' \times 10'$ and centered on the target, which expediently assisted our identification of the object in prediscovery archival data. Neighboring background stars have FWHM values between $2\overset{''}{.}0$ and $2\overset{''}{.}3$.

2.4. VLT Survey Telescope

We located comet C/2019 E3 in VST data from two nights in 2013 April obtained in the *g* and *r* filters at the 2.6 m VST at Cerro Paranal, Chile, with OmegaCAM, which consists of 32 2k×4k e2v CCD chips rendering an overall angular area of $\sim 1 \times 1$ deg^2 at an angular resolution of $0\overset{''}{.}21$ pixel^{-1} (Kuijken et al. 2002). As the observations returned by SSOIS were only raw images, we retrieved the corresponding bias and flat frames from the ESO Science Archive Facility and performed standard calibration. We measured the seeing during the observations, which varied between $1\overset{''}{.}0$ and $1\overset{''}{.}2$.

2.5. Zwicky Transient Facility

Together with SSOIS at CADC and the Moving Object Search Tool (Masci et al. 2019) at IPAC,[6] we collected fortuitous ZTF observations from three different nights in 2018 April to May in which the comet was found by visual inspection. These images at a pixel scale of $1\overset{''}{.}01$ were obtained by the wide-field ZTF camera, which is comprised of 16 e2v 6k × 6k CCDs covering a ~ 47 deg^2 field of view on the 1.2 m Samuel Oschin Schmidt Telescope at the Palomar Observatory, USA, during its all-sky survey (Bellm et al. 2019; Graham et al. 2019; Masci et al. 2019). Field stars in the images were measured to have seeing FWHM varying within a range of $2\overset{''}{.}2$–$2\overset{''}{.}9$.

---

[6] https://irsa.ipac.caltech.edu/applications/MOST/

We tabulate detailed information of the serendipitous archival observations along with the viewing geometry of the comet in Table 1.

3. Results

3.1. Morphology

Visually inspecting the observed morphology of C/2019 E3 in the serendipitous archival data, we found that the comet displayed no prominent tail but maintained a symmetric appearance in general (see Figure 1), regardless of the orbital plane angle at which it was observed (see Table 1). In particular, this symmetric morphology largely remained even for the PS1 data obtained from 2018 March 8 when the Earth was practically within the orbital plane of the comet, although only one image from the imaging sequence managed to escape from an artifact caused by bleeding of a nearby bright star. Only in the post-discovery DECam data taken from 2019 June 8 could we notice hints of elongation in the appearance of the comet (see Figure 1). The insensitivity of the comet's morphology to the changing orbital plane angle implies that its observed dust environment was dominated by relatively large-sized particles, as they are less susceptible to solar radiation pressure than their smaller counterparts. Otherwise, we would expect the comet to be extended considerably in its orbital plane in comparison to the out-of-plane direction.

We examined the radial brightness profile of the comet in 2019 when it had the best signal-to-noise ratios in the available archival data. A power-law surface brightness model was fitted to the observations in an annular region between $1''$ and $3''$ in radius from the comet after the sky background was removed, whereby we obtained the best-fit logarithmic surface brightness slope of the comet. The values were found to be statistically consistent with the one in steady state (see Figure 2). We verified that adjusting the fitted region did not affect the results beyond the noise level. Therefore, we are confident to conclude that the mass loss of the comet was most likely in a steady state, suggestive of activity driven by sublimation. Given that temperature at the observed range of heliocentric distances would be too low for water ice to sublimate, we prefer sublimation of supervolatiles such as carbon monoxide (CO) and carbon dioxide (CO_2) as the activity mechanism at play.

The observed morphology of C/2019 E3 has a close resemblance to that of C/2017 K2 (PANSTARRS), another ultradistant comet whose dust coma was reported to be primarily comprised of submillimeter-scaled grains ejected in a protracted manner at speeds of $\lesssim 3$ m s^{-1} at similar heliocentric distances (Hui et al. 2018; Jewitt et al. 2019). Therefore, we conjectured that the physical properties of the dust environment of C/2019 E3 strongly resembled that of C/2017 K2. In Section 4.1, we will detail the application of our Monte Carlo dust model to investigate the physical properties of the dust environment of C/2019 E3.

3.2. Photometry

The serendipitous archival images containing C/2019 E3 were photometrically calibrated using ATLAS Refcat2 (Tonry et al. 2018). We transformed measurements in the PS1 photometric system to the SDSS system following Tonry et al. (2012). Photometry of C/2019 E3 in archival data from the five telescopes was carried out using circular apertures having fixed linear radii from 2.5×10^4 to 4×10^4 km at a step

Table 1
Archival Serendipitous Observations and Viewing Geometry of Comet C/2019 E3 (ATLAS)

Date (UTC)	Archival Observations				Viewing Geometry						
	Facility	Filter	# images	Exposure (s)	$r_{\rm H}$ (au)[a]	Δ (au)[b]	α (°)[c]	ε (°)[d]	$\theta_{-\odot}$ (°)[e]	$\theta_{-\mathbf{V}}$ (°)[f]	ψ (°)[g]
2012 Mar 19	PS1	w	1	45	23.009	22.037	0.5	167.2	90.5	17.8	−0.5
2012 Nov 25	PS1	w	2	45	22.062	22.324	2.5	73.3	291.0	14.5	+2.4
2013 Feb 14	PS1	r	2	40	21.756	20.853	1.1	155.5	311.1	16.1	+1.0
2013 Feb 15	PS1	w	3	45	21.752	20.843	1.0	156.5	312.0	16.1	+0.9
2013 Mar 5	PS1	w	4	45	21.685	20.704	0.4	171.1	1.1	17.0	+0.1
2013 Apr 1	DECam	z	1	100	21.584	20.680	1.2	154.2	94.9	18.4	−1.1
2013 Apr 3	DECam	z	2	100	21.576	20.687	1.2	152.2	96.4	18.5	−1.2
2013 Apr 3	PS1	w	4	45	21.575	20.687	1.2	152.0	96.5	18.5	−1.2
2013 Apr 4	OmegaCAM	g	2	50	21.573	20.690	1.3	151.3	97.0	18.5	−1.3
2013 Apr 7	OmegaCAM	r	2	45	21.561	20.703	1.4	148.3	98.8	18.6	−1.4
2014 Feb 20	DECam	i	3	160	20.354	19.431	1.0	158.5	325.7	16.3	+0.8
		g	3	160							
2014 Feb 20	PS1	i	1	45	20.353	19.428	1.0	158.8	326.3	16.3	+0.8
2014 Feb 28	PS1	w	4	45	20.323	19.365	0.7	164.8	345.4	16.8	+0.4
2014 Mar 11	DECam	i	4	30	20.283	19.311	0.6	167.6	32.0	17.4	−0.2
		g	2	30							
2014 Dec 10	PS1	i	2	45	19.244	19.276	2.9	86.7	292.7	14.1	+2.9
2014 Dec 18	PS1	i	2	45	19.214	19.111	2.9	94.5	294.8	14.2	+2.9
2015 Jan 2	PS1	i	1	45	19.158	18.810	2.8	109.3	299.1	14.4	+2.7
2015 Jan 16	PS1	r	2	45	19.105	18.548	2.5	123.2	304.2	14.8	+2.4
2015 Jan 18	PS1	w	4	45	19.097	18.513	2.4	125.2	305.0	14.9	+2.3
2015 Jan 20	PS1	w	4	45	19.090	18.481	2.4	127.1	305.9	14.9	+2.2
2015 Jan 22	PS1	w	2	45	19.082	18.447	2.3	129.0	306.9	15.0	+2.2
2015 Mar 22	PS1	w	4	45	18.860	17.928	1.1	158.8	62.1	18.2	−0.8
2016 Jan 11	PS1	z	1	30	17.751	17.291	2.8	116.5	304.9	14.7	+2.7
2016 Feb 12	PS1	w	1	45	17.632	16.811	1.8	145.3	328.7	16.2	+1.4
2016 Mar 28	PS1	r	4	45	17.464	16.587	1.6	150.7	67.2	19.1	−1.2
2016 Apr 3	PS1	w	4	45	17.442	16.601	1.8	146.4	75.9	19.4	−1.5
2016 May 21	PS1	i	3	45	17.263	16.984	3.3	104.4	107.5	21.3	−3.2
2017 Apr 16	SkyMapper	g	1	100	16.048	15.344	2.6	133.2	84.0	21.0	−2.3
		r	1	100							
		i	1	100							
2017 Apr 22	SkyMapper	r	1	100	16.026	15.381	2.8	128.5	89.1	21.3	−2.6
2017 Apr 25	PS1	w	4	45	16.016	15.402	2.9	126.2	91.2	21.4	−2.7
2017 Apr 28	PS1	w	2	45	16.005	15.425	3.0	123.7	93.4	21.6	−2.9
2018 Mar 8	PS1	w	4	45	14.883	14.064	2.2	144.4	20.2	19.6	+0.0
2018 Apr 27	ZTF	g	1	30	14.709	14.150	3.3	122.1	89.2	23.1	−3.1
2018 May 11	ZTF	g	1	30	14.660	14.261	3.7	111.4	99.6	23.6	−3.6
2018 May 22	ZTF	r	1	30	14.622	14.365	3.9	102.8	106.5	23.9	−3.8
2019 Apr 5	PS1	w	4	45	13.554	12.887	3.2	130.2	62.7	24.2	−2.0
2019 Jun 8	DECam	g	1	90	13.347	13.320	4.4	89.3	118.7	26.6	−4.3

Notes.
[a] Heliocentric distance.
[b] Observer-centric distance.
[c] Phase angle.
[d] Solar elongation.
[e] Position angle of antisolar direction projected in the observer's plane of the sky.
[f] Position angle of negative heliocentric velocity projected in the observer's plane of the sky.
[g] Orbital plane angle. Negative values indicate the observer is below the orbital plane of the comet.

size of 5000 km projected at the distance of the comet. The benefit of utilizing such apertures is that, in spite of the observer-centric distance of the comet varying as a function of time, the sampled region around the comet remained fixed, thereby avoiding the introduction of unnecessary influences due to the changing viewing geometry as much as possible. Figure 3 shows the apparent magnitude of the comet enclosed by an aperture of 3×10^4 km in radius against time in the corresponding SDSS-system bandpasses, in which the magnitude uncertainties were standard deviations of multiple measurements from the same telescopes and filters in the same nights, or in cases where only single measurements were available, propagated from Poisson statistics and errors in zero points of images. During the observed period, the comet basically steadily brightened on its way to perihelion, exhibiting no compelling evidence of outbursts in brightness.

The observed steady brightening of C/2019 E3 may imply its gradually increasing total effective scattering cross section of dust. We computed this quantity using the r-band data points of our measurements through the following equation:

$$\Xi_e = \frac{\pi}{p_r \phi(\alpha)} \left(\frac{r_H \Delta}{r_\oplus} \right)^2 10^{0.4(m_{\odot,r} - m_r)}, \qquad (1)$$

where m_r is the apparent r-band magnitude of the comet, $m_{\odot,r} = -26.93$ is the apparent r-band magnitude of the Sun at mean heliocentric distance of Earth $r_\oplus = 1$ au (Willmer 2018), r_H and Δ respectively are the heliocentric and observer-centric distances of the comet, and ϕ and p_r respectively are the dimensionless phase dependency as a function of phase angle α and the r-band geometric albedo of dominant dust grains comprising the coma of the comet. As there is no observation that can possibly provide constraints on the latter two quantities, we had to assume a nominal value of $p_r = 0.05$ for the geometric albedo (e.g., Levasseur-Regourd et al. 2018) and adopt a linear phase function with typical phase coefficient $\beta_\alpha = 0.03 \pm 0.01$ mag degree^{-1} (Meech & Jewitt 1987) for optically dominant dust grains in the coma. The result is plotted against heliocentric distance in Figure 4, which shows that the effective scattering cross section of dust generally increased as the comet approached the Sun, as expected. We used the power-law form of $\Xi_e \sim r_H^\gamma$, where γ is a constant power-law index, to obtain the least-squares fit for the data set. The best-fit power-law index for the heliocentric distance dependency is $\gamma = -1.5 \pm 0.4$, where the stated uncertainty is the 1σ formal error propagated from the counterparts in the measurements. We note that the obtained value is not statistically different from the one for C/2017 K2, another ultradistant comet, at a similar range of heliocentric distances ($\gamma = -1.14 \pm 0.05$; Jewitt et al. 2021). On the other hand, the behavior of C/2019 E3 was dissimilar to that of the other two known ultradistant comets C/2010 U3 and C/2014 UN$_{271}$, both of which exhibited obvious outbursts at similar preperihelion heliocentric distances (Hui et al. 2019; Kelley et al. 2022), rendering the power-law model inapplicable.

The multiband observations of the comet allowed for measurements of its color at several epochs (see Table 2). Due to the large uncertainty in the photometric measurements, we found no compelling evidence of radial gradients in the color of the coma. Unfortunately, only the $g - i$ color of the comet was

available from multiple epochs, which are highly unevenly spaced in time—the first two were obtained from two nights merely a month apart from each other, and the third one was measured over three years later after the first pair. From these measurements, we saw no evidence of temporal variation in the $g - i$ color of the comet statistically beyond the noise level. Therefore, we computed the weighted mean color indices of the comet from the repeated photometric measurements regardless of the used photometric apertures. We obtained $g - i = +0.78 \pm 0.13$, $g - r = +0.38 \pm 0.05$, $r - i = +0.41 \pm 0.08$, and $r - z = +0.49 \pm 0.06$ (see also Table 2). In comparison to the solar colors, $g - r = +0.46 \pm 0.03$, $r - i = +0.12 \pm 0.03$, and $r - z = +0.15 \pm 0.03$, which we derived from Willmer (2018), while the color of the comet in $g - r$ appeared to be similar to that of the Sun given the uncertainty, at longer wavelengths the comet was likely redder than the Sun. We also compared the color of C/2019 E3 to those of other long-period comets as well as short-period ones, reported by Solontoi et al. (2012), finding that, while the comet appeared to have a somewhat bluer color in $g - r$ than typical comets, the colors of the comet in other wavelength intervals are fully comparable.

3.3. Orbit Determination

We exploited field stars to solve plate constants of the serendipitous archival data referenced to the Gaia Data Release 2 and 3 catalogs (Gaia Collaboration et al. 2018, 2023), during which process the field stars were simply treated as bidimensional symmetric Gaussians to be fitted. Despite the fact that none of the archival data tracked the apparent nonsidereal motion of the comet, the motion was slow enough that the optocenters of the comet remained circularly symmetric enough. Thus, we also simply treated the comet as a bidimensional symmetric Gaussian, whereby the best-fitted pixel coordinates of the centroid of the comet were obtained. We then transformed the pixel coordinates of the comet to the J2000 equatorial coordinate system in terms of R.A. and decl. Meanwhile, the corresponding uncertainties were obtained by propagating the counterparts in centroiding and astrometric calibration, based upon which our astrometry was properly weighted. In addition, we included more recent astrometric measurements of the comet returned by the Minor Planet Center Database Search.[7] As the data set from the Minor Planet Center contained no information on the measurement uncertainties and consisted of astrometric reduction to a mix of various star catalogs, we debiased and assigned a weighting scheme for the data following descriptions detailed in Eggl et al. (2020) and Vereš et al. (2017), respectively. We then fed the astrometric observations with the adopted weighting scheme into the orbit determination package `Find_Orb`,[8] which incorporated gravitational perturbations from the eight major planets, Pluto, the Moon, and the 16 most massive asteroids in the main belt, as well as relativistic effects. Planetary and lunar ephemeris DE440 (Park et al. 2021) was exploited to speed up the N-body integration process of the package. Our measurements with observed-minus-calculated ($O - C$) astrometric residuals greater than the 3σ level were slightly downweighted accordingly, whereas six of the measurements from the Minor Planet Center were simply discarded, because the latter all have $O - C$ residuals greater than a few arcseconds, at least an order

---

[7] https://minorplanetcenter.net/db_search
[8] The orbit determination package is developed by B. Gray, publicly available at https://github.com/Bill-Gray/find_orb.
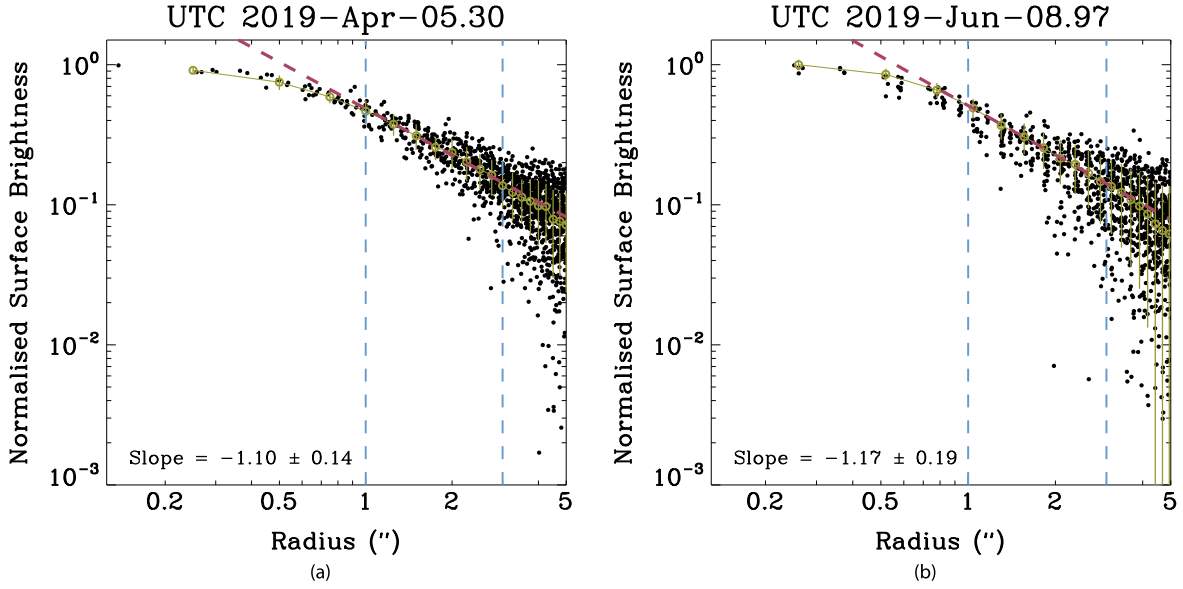
Figure 2. Normalized radial surface brightness profiles of C/2019 E3 from (a) 2019 April 5 in the PS1 data and (b) 2019 June 8 in the DECam data. Azimuthally mean values are plotted in olive, with the best-fit power-law radial profiles plotted as pink dashed lines. In each panel, the inner and outer radii of the fitted annular region are marked by two vertical blue lines, and the value of the best-fit logarithmic surface brightness slope is given in the lower left corner.
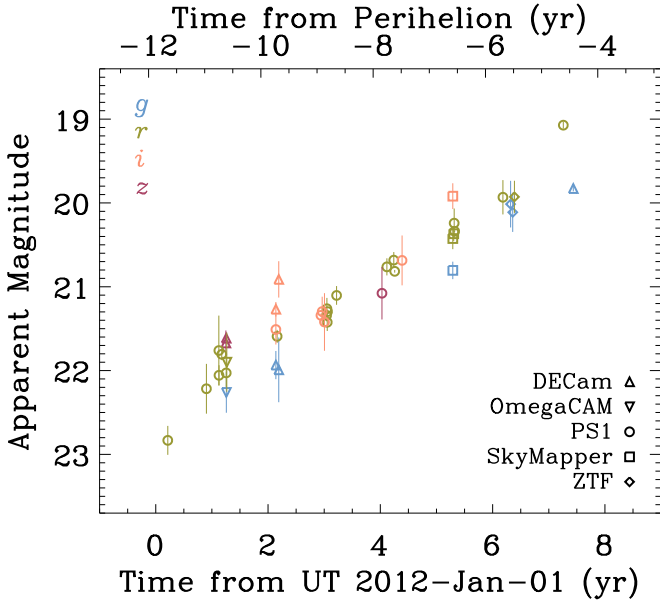
Figure 3. Apparent magnitude of comet C/2019 E3 in multiple bands in the SDSS system measured with a 3×10^4 km radius aperture vs. time. Data points are color coded according to the calibrated photometric bands and plotted in different symbols representing different facilities as shown in the legends. In general, the apparent brightness of the comet increased steadily as it approached perihelion.

Figure 4. Effective scattering cross section of dust as a function of heliocentric distance, calculated from r-band data points measured with an aperture of 3×10^4 km in radius. Data points in different symbols correspond to measurements from different facilities. The dotted curve is the best-fit power law with heliocentric distance for the effective scattering cross section of dust. The overall trend is that the effective scattering cross section of dust increased monotonically as the comet approached the Sun.

of magnitude worse than the former. We tabulate the best-fitted osculating heliocentric orbital elements in Table 3. It is worth pointing out that the current perihelion distance of the comet is the third largest for known comets after C/2003 A2 (Gleason) and C/2014 UN$_{271}$ (with $q = 11.4$ au and 10.9 au, respectively, according to solutions by JPL Horizons).

4. Discussion

4.1. Dust Properties

We applied our Monte Carlo dust dynamical code to simulate the dust morphology of C/2019 E3 from a list of epochs observed in good quality at various orbital plane angles, as a way to probe the physical properties of its dust environment. The model assumed that dust grains of spherical shape were ejected from the nucleus due to sublimative activity, forming a cone-shaped jet symmetric about the Sun–comet axis toward the Sun, at a range of nonzero terminal ejection speeds following an empirical relation of (e.g., Ishiguro 2008)

$$V_{\mathrm{ej}} = V_{\mathrm{ej},0} \sqrt{\left(\frac{r_{\oplus}}{r_{\mathrm{H}}}\right)\left(\frac{\mathfrak{a}_{\mathrm{d},0}}{\mathfrak{a}_{\mathrm{d}}}\right)}. \qquad (2)$$

Table 2
Color Measurements of Comet C/2019 E3 (ATLAS)

Date (UTC)	Facility	Color Index	Color Measurement			
			Photometric Aperture Radius (10^4 km)			
			2.5	3.0	3.5	4.0
2013 Apr 3	DECam & PS1	$r - z$	$+0.41 \pm 0.17$	$+0.44 \pm 0.09$	$+0.52 \pm 0.08$	$+0.55 \pm 0.13$
2014 Feb 20	DECam	$g - i$	$+0.67 \pm 0.19$	$+0.68 \pm 0.20$	$+0.71 \pm 0.20$	$+0.67 \pm 0.29$
2014 Mar 11	DECam	$g - i$	$+1.08 \pm 0.44$	$+1.05 \pm 0.43$	$+0.98 \pm 0.48$	$+1.03 \pm 0.25$
2017 Apr 16	SkyMapper	$g - r$	$+0.38 \pm 0.17$	$+0.42 \pm 0.16$	$+0.41 \pm 0.15$	$+0.32 \pm 0.16$
		$r - i$	$+0.51 \pm 0.20$	$+0.39 \pm 0.20$	$+0.30 \pm 0.20$	$+0.42 \pm 0.21$
		$g - i$	$+0.89 \pm 0.19$	$+0.82 \pm 0.19$	$+0.71 \pm 0.20$	$+0.73 \pm 0.19$
Weighted Mean		$g - r$	$+0.38 \pm 0.05$			
		$g - i$	$+0.78 \pm 0.13$			
		$r - i$	$+0.41 \pm 0.08$			
		$r - z$	$+0.49 \pm 0.06$			

Note. The reported uncertainties are weighted standard deviations of repeated measurements. Weighted mean colors of the comet were computed from measurements using different photometric apertures. For comparison, here we list also the median colors of comets reported by Solontoi et al. (2012): $g - r = +0.57 \pm 0.05$, $r - i = +0.22 \pm 0.07$, and $i - z = +0.09 \pm 0.07$.

Here, $\mathfrak{a}_d$ is the grain radius, $\mathfrak{a}_{d,0} = 5$ mm is the referenced grain radius, and $V_{ej,0}$ is the terminal ejection speed of reference-sized dust at $r_\oplus$ from the Sun. For simplicity, the acceleration process of dust grains to terminal speeds was ignored, such that they instantaneously reached terminal speeds after ejection. The dimension of the nucleus was ignored in the model as well. Afterward, each of the dust grains was considered to be dominantly subject to the solar radiation pressure force and the solar gravitational force, whose ratio is inversely proportional to $\rho_d \mathfrak{a}_d$ (ρ_d is the bulk density of dust, assumed to be 1 g cm^{-3}). The gravity of the nucleus was neglected. We used a power-law size distribution for the number of dust grains, i.e., $d\mathcal{N} \propto \mathfrak{a}_d^{-\gamma} d\mathfrak{a}_d$ ($d\mathcal{N}$ is the number of dust grains having radii from $\mathfrak{a}_d$ to $\mathfrak{a}_d + d\mathfrak{a}_d$, and γ is the power-law index of the size distribution), in a dust-size range of $\mathfrak{a}_{d,min} \leqslant \mathfrak{a}_d \leqslant \mathfrak{a}_{d,max}$. The production rate was assumed to be inversely proportional to the square of the heliocentric distance. Motions of the simulated ejected particles alongside the nucleus itself were integrated from the time of ejection to the corresponding observed epochs in our implemented version of mercury6 (Chambers 1999). Our code then transformed the Cartesian heliocentric states of the nucleus and particles to topocentric ones, with light-travel time corrected. After adopting the image scales of the actual observations selected for modeling, we thereby attained model images of the comet to be compared against actual observations. Earlier versions of our dust dynamical code have been previously applied for various active small Solar System bodies, including another ultradistant comet C/2017 K2 (Hui et al. 2018; Jewitt et al. 2019).

Unfortunately, owing to the faintness of the comet and the quality of the archival data, we could not simply treat all the relevant physical parameters of the dust environment as free parameters to be solved by straightforwardly fitting the morphology of the comet. Rather, we started with physical parameters of dust grains similar to those of comet C/2017 K2 in Hui et al. (2018) and Jewitt et al. (2019) and tweaked them manually when necessary. Given our earliest archival observation of the comet in 2012, we set the onset time of activity to be

Table 3
Best-fit Orbital Solution for Comet C/2019 E3 (ATLAS)

Quantity		Value
Eccentricity	e	0.9986052(37)
Perihelion distance (au)	q	10.312984(13)
Semimajor axis (10^3 au)	a	7.394(19)
Inclination (°)	i	84.2995123(82)
Argument of perihelion (°)	ω	280.70139(12)
Longitude of ascending node (°)	Ω	347.2298923(47)
Time of perihelion (TDT)[a]	t_p	2023 Nov 15.3135(28)
Observed arc		2012 Mar 19–2024 Jan 19
Number of observations used (discarded)		789 (8)
Residual rms (″)		0.462
Normalized residual rms		0.574

Notes. The osculating orbit is referenced to the heliocentric J2000 ecliptic at epoch TDT 2023 January 19.0 = JD 2460328.5. Here, numbers in parentheses of the orbital elements are 1σ formal errors of the corresponding parameters.
[a] The uncertainty is in days.

early 2011. We have verified that adopting even earlier epochs or slightly later epochs had no appreciable effect in the resulting modeled morphology. The maximum grain size and the power-law index of the dust-size distribution were found to have no significant effect on the modeled dust morphology either, as long as the latter parameter satisfies $\gamma > 3$, which holds for the great majority of comets (Fulle 2004), and so we simply adopted $\mathfrak{a}_{d,max} = 1$ cm and a nominal value of $\gamma = 3.5$ (e.g., Agarwal et al. 2023). On the contrary, the modeled morphology is mostly sensitive to the input minimum dust size and ejection speeds, as expected. By employing step sizes of 1 mm and 0.1 m s^{-1} for $\mathfrak{a}_{d,min}$ and $V_{ej,0}$, respectively, we ended up obtaining models with particles having $\mathfrak{a}_{d,min} = 2$ mm and $V_{ej,0} = 1.2$ m s^{-1} released from the sunlit hemisphere of the nucleus starting since 2011 vividly reproducing the observed morphology of the comet (see Figure 5, to be compared with observations in Figure 1). Scaling with the obtained reference ejection speed using Equation (2), our model suggests that the observed dust morphology of the comet was likely formed by protracted ejections of dust of mm-scale and greater at speeds

$\lesssim 0.4 \, \mathrm{m \, s^{-1}}$ in the observed range of heliocentric distances. As a comparison, Hui et al. (2018) and Jewitt et al. (2019) reported that the optically dominant dust in the coma of C/2017 K2 was at least submillimeter-scaled and had ejection speeds $\lesssim 4 \, \mathrm{m \, s^{-1}}$ at similar heliocentric distances. As such, the results from our Monte Carlo dust modeling for C/2019 E3 are in line with the scenario where the observed activity of the comet is driven by sublimation of supervolatiles, the same activity mechanism as for C/2017 K2.

4.2. Activity

The total mass-loss rate of C/2019 E3 driven by steady-state ejection of dust is given by the total mass within the region enclosed by some photometric aperture divided by the aperture crossing time of dust, i.e.,

$$\dot{\mathcal{M}}_d \approx \frac{4 \rho_d \bar{a}_d \overline{V}_{ej} \Xi_e}{3 \ell}. \quad (3)$$

Here, $\bar{a}_d$, and $\overline{V}_{ej}$ respectively are the mean radius and mean ejection speed of dust particles in the coma, and ℓ is the aperture radius projected at the distance of the comet. Unfortunately, because we could not robustly determine the maximum size or the size distribution of ejected dust (Section 4.1), we instead varied the mean dust radius from the minimum size and scaled the corresponding ejection speed using Equation (2). The results with the best-fit power-law form of the effective scattering cross section of dust as a function of heliocentric distance are plotted in Figure 6. Also plotted are net mass-loss rates of dust grains having various mean radii, which we calculated from

$$\begin{aligned} \frac{\Delta \mathcal{M}_d}{\Delta t} &\approx \frac{4}{3} \rho_d \bar{a}_d \frac{\Delta \Xi_e}{\Delta t} \\ &= -\frac{4}{3} \rho_d \bar{a}_d \left(\frac{\Delta \Xi_e}{\Delta r_H} \right) \\ &\quad \cdot \frac{1}{r_H} \sqrt{\mu_\odot \left(\frac{r_H - q}{q} \right) [(1 + e) q - (1 - e) r_H]} \quad (4) \\ &\approx -\frac{4}{3} \rho_d \bar{a}_d \left(\frac{\Delta \Xi_e}{\Delta r_H} \right) \frac{\sqrt{2 \mu_\odot (r_H - q)}}{r_H}. \quad (5) \end{aligned}$$

Here, $\mu_\odot \triangleq GM_\odot$, in which G is the gravitational constant and $M_\odot$ is the mass of the Sun, is the mass parameter of the Sun, and we applied the chain rule to arrive at Equation (4), which can be further approximated to Equation (5) with a near-parabolic eccentricity of $e \approx 1$. Given the unknowns and uncertainties in the pertinent physical parameters of dust grains, the results from these calculations shown in Figure 6 are likely no better than order-of-magnitude estimates. During the observed timespan, the comet experienced a total dust mass-loss rate of $\gtrsim 10^2 \, \mathrm{kg \, s^{-1}}$ and net mass-loss rate of $\gtrsim 10 \, \mathrm{kg \, s^{-1}}$ even at heliocentric distance $r_H \gtrsim 20$ au. We note that such a level of activity was comparable to that of C/2017 K2 (PANSTARRS) at similar distances from the Sun (total mass-loss rate $\gtrsim 200 \, \mathrm{kg \, s^{-1}}$; Hui et al. 2018; Jewitt et al. 2019).

In the following, we proceed to estimate the minimum size of the nucleus that would be required to sustain the activity of C/2019 E3. Given the great heliocentric distances of the comet, the protracted mass production is mostly consistent with activity driven by sublimation of supervolatiles such as CO and CO_2, as in the cases of the other three ultradistant comets. Adopting a ratio of dust-to-gas mass production rates of $\mathcal{X}$, we can relate the minimum sublimating area to the total mass-loss rate of dust as

$$\mathcal{A}_s = \frac{\dot{\mathcal{M}}_d}{\mathcal{X} f_s}. \quad (6)$$

Here, f_s is the mass flux of some sublimating substance, which can be numerically solved from the following energy equilibrium equation:

$$(1 - A_B) S_\odot \left(\frac{r_\oplus}{r_H} \right)^2 \cos \zeta = \epsilon \sigma T^4 + L(T) f_s(T). \quad (7)$$

The left-hand side represents insolation at the nucleus, which is converted to energy spent in thermal reradiation and sublimation (the two terms on the right-hand side). In the above equation, A_B is the Bond albedo of the nucleus, $S_\odot = 1361 \, \mathrm{W \, m^{-2}}$ is the solar constant, $\cos \zeta$ is the effective projection coefficient for the surface in a range of $\cos \zeta \in [1/4, 1]$, with the upper and lower bounds corresponding to subsolar and isothermal scenarios, respectively, $\sigma = 5.67 \times 10^{-8} \, \mathrm{W \, m^{-2} \, K^{-4}}$ is the Stefan–Boltzmann constant, ϵ and T are the surface emissivity and equilibrium temperature, respectively, and L is the latent heat of the sublimating substance varying with temperature. To solve Equation (7) for the mass fluxes of outgassing CO and CO_2, we assumed a conservative ratio of dust-to-gas mass production rates $\mathcal{X} = 5$, as in Jewitt et al. (2019), and values of $A_B = 0.01$ and $\epsilon = 0.9$, both of which are typical for cometary nuclei (Kelley et al. 2017; Knight et al. 2023), and we adopted the empirical sublimation models of Fray & Schmitt (2009). In the subsolar scenario, the minimum diameter of the cometary nucleus is simply the diameter of the equal-area circle, whereas in the isothermal case, it is given by the diameter of a sphere having the same surface area as the minimum sublimating area yielded by Equation (6). We plot the results for CO and CO_2 respectively in the left and right panels of Figure 7, in which we immediately notice that the isothermal sublimation models of CO_2 should be rejected, in that they all predict unreasonably enormous nucleus sizes for the comet. On the other hand, results from the subsolar model with CO_2 are not appreciably different from those from the subsolar and isothermal models with CO, which themselves are nearly indistinguishable from each other. Aside from these models, we also adopted an empirical model by Womack et al. (2017) that is consistent with the CO measurements of comet C/1995 O1 (Hale–Bopp) and Centaur 29P/Schwassmann–Wachmann at heliocentric distances from ∼4 to 10 au. Extrapolating the empirical model to greater heliocentric distances, we find that the estimated diameter for the nucleus of C/2019 E3 is ∼80 km, at least an order of magnitude greater than our results with the sublimation models by Fray & Schmitt (2009). The discrepancy may imply that either the nucleus of the comet is even larger than those of C/1995 O1 and 29P, which were reported to have effective nucleus radii of ∼37 km and 30 km, respectively (Szabó et al. 2012; Schambeau et al. 2015, 2021), or that the
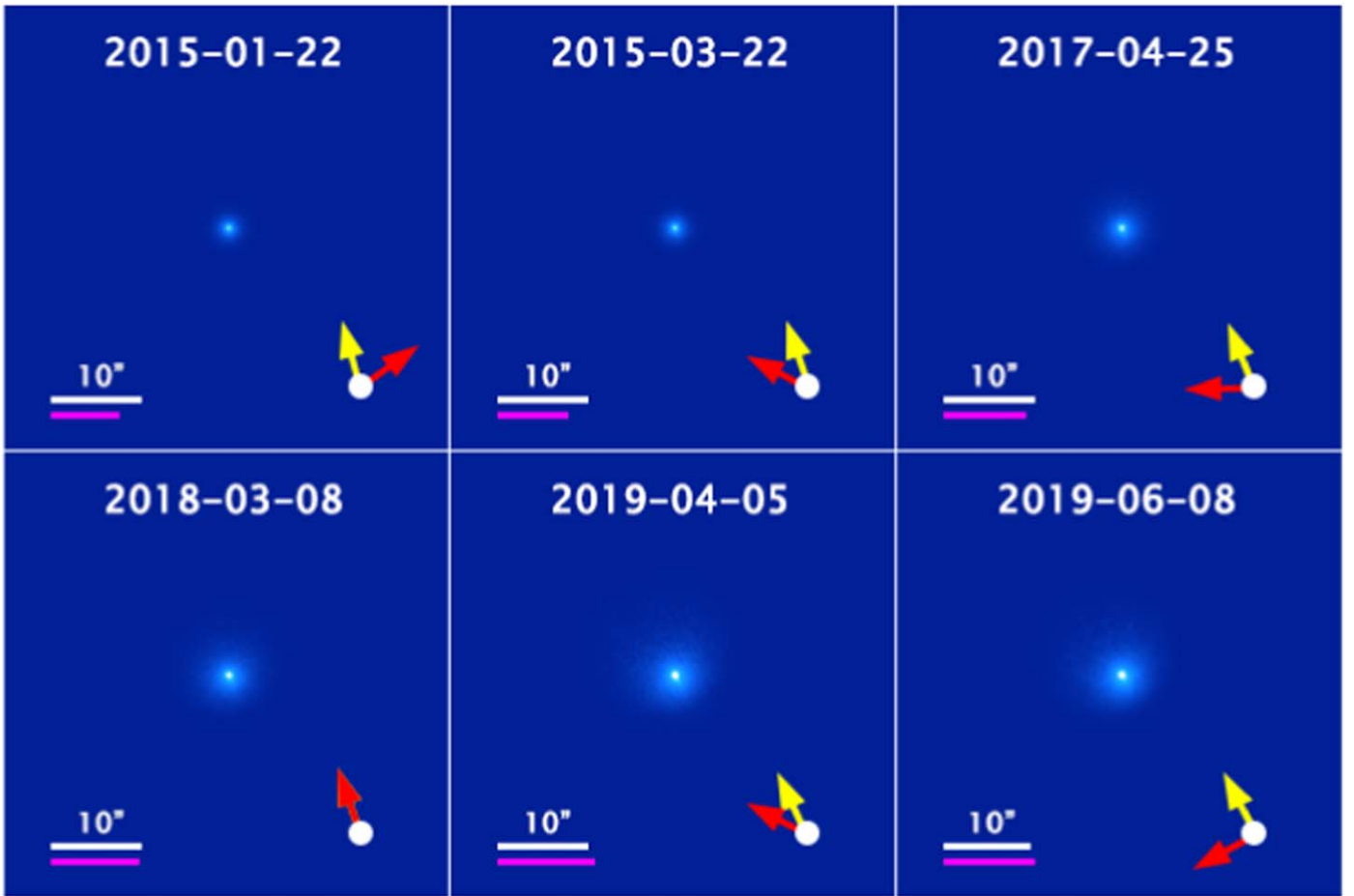
Figure 5. Monte Carlo dust models of comet C/2019 E3 at six of the selected epochs. All of the images are scaled logarithmically. In each panel, the red and yellow arrows mark the position angles of the antisolar direction and the negative heliocentric velocity projected in the plane of the sky, respectively, and two scale bars of $10''$ in apparent length (labeled) and 10^5 km projected at the observer-centric distance of the comet are shown in white and magenta, respectively. J2000 equatorial north is up and east is left.

latter two objects would be less active than was C/2019 E3 at heliocentric distances $r_H \gtrsim 10$ au. On the whole, we are confident to conclude that the nucleus of C/2019 E3 is most likely greater than $\sim$3 km in diameter.

4.3. Orbital Evolution

It is of scientific interest to understand why C/2019 E3 could be so active even at great distances from the Sun and whether this behavior implies that it is one of the most pristine objects in our Solar System. As the thermophysical status of the comet is closely associated with its dynamical history, we investigated its orbital evolution and examined whether or not C/2019 E3 has previously entered the planetary region, i.e., whether it is dynamically old or new, and if the observed activity could be attributed to retained heat from the previous perihelion return. We created 5000 Monte Carlo clones of the nominal orbit based on the best-fit orbital elements and the covariance matrix obtained from the orbit determination detailed in Section 3.3, all of which, together with the nominal orbit, were integrated backward in time using our modified version of mercury6 until they reach preperihelion heliocentric distance $r_H = 250$ au, beyond which planetary perturbations are negligible. The osculating orbit when at
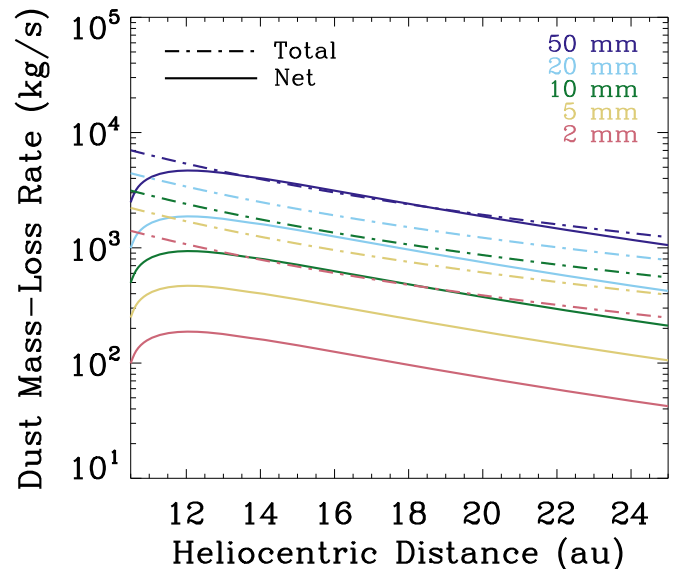
Figure 6. Total and net mass-loss rates of comet C/2019 E3 vs. heliocentric distance (dashed–dotted and solid curves, respectively) assuming different effective radii of dust grains (plotted in different colors). The best-fit effective scattering cross section of dust in the power-law form vs. heliocentric distance (see Section 3.2) was used.
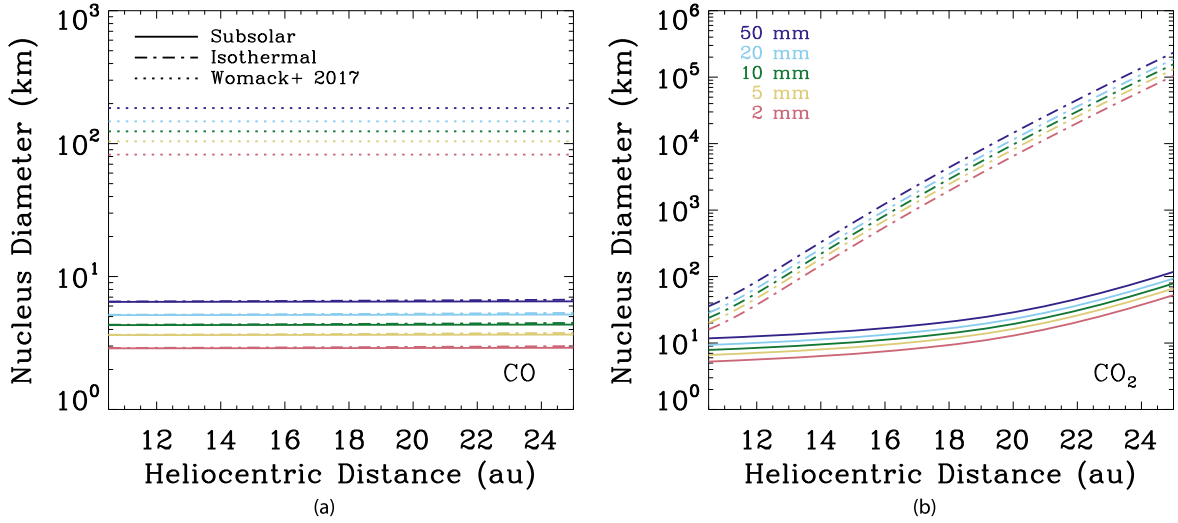
Figure 7. Lower limits to the nucleus diameter of C/2019 E3 as functions of heliocentric distance assuming the observed activity is driven by sublimation of CO (a) and CO_2 (b). Results in subsolar and isothermal scenarios are plotted as solid and dashed–dotted curves, respectively, in different colors representing different effective sizes of dust grains used for the computation. We conservatively assumed $\mathcal{X} = 5$ for the ratio of the dust-to-gas mass production rates in the calculation. In addition, we adopted an empirical model by Womack et al. (2017) that is consistent with the CO measurements of comet C/1995 O1 (Hale–Bopp) and Centaur 29P/Schwassmann–Wachmann in the left panel, extrapolating it to greater heliocentric distances.

preperihelion heliocentric distance $r_H = 250$ au is termed the "original" orbit of the comet, following the definition by Dybczyński (2001). The N-body integration took into account perturbations from the eight major planets, Pluto, the Moon, and the 16 most massive asteroids in the main belt, the heliocentric states of which were taken from DE440. Also included in the force model were post-Newtonian corrections and the Galactic tide assuming a local stellar density of $\rho_* = 0.1 M_\odot \text{ pc}^{-3}$ in the solar neighborhood and using the formalism detailed in Appendix A, which was derived based on the work of Fouchard et al. (2005). We list the orbital elements and the corresponding uncertainties of the original orbit of C/2019 E3 computed from the 5001 orbital clones in Table 4, with reference to the Solar System barycenter in the J2000 ecliptic coordinate system. Then, starting with the obtained original orbit and assuming gravitational perturbations from nearby passing stars are unimportant, we adopted an analytic approach to evaluate the change in the periapsis distance of the comet between the previous and current returns in the Solar System barycentric reference system.

The Hamiltonian for a comet orbiting around the barycenter of the Solar System under the influence of the tidal potential from the Galactic disk is

$$H = -\frac{\mu_0}{2a} + \underbrace{2\pi G \rho_* \left[\frac{a(1 - e^2)}{1 + e \cos f} \sin (f + \tilde{\omega}) \sin \tilde{\imath} \right]^2}_{-\mathcal{R}}, \quad (8)$$

where μ_0 is the mass parameter of the Solar System barycenter, f is the true anomaly of the comet, a, e, $\tilde{\imath}$, and $\tilde{\omega}$ are the semimajor axis, eccentricity, orbital inclination, and argument of periapsis, respectively, in the Solar System barycentric Galactic frame, and $\mathcal{R}$ is the disturbing function due to the Galactic tide, whose influence parallel to the Galactic plane is neglected (Heisler & Tremaine 1986). The Keplerian orbital elements in the Galactic reference frame were converted from the counterparts in the ecliptic reference frame (see

Table 4
Original and Future Orbits of Comet C/2019 E3 (ATLAS)

Quantity		Original	Future
Eccentricity	e	0.9997079(37)	0.9994170(37)
Periapsis distance (au)	q	10.313056(13)	10.308711(13)
Semimajor axis (10^4 au)	a	3.532(44)	1.768(11)
Reciprocal of semimajor axis (10^{-5} au^{-1})	a^{-1}	2.832(36)	5.655(36)
Inclination (°)	i	84.2820905(81)	84.2848023(81)
Argument of periapsis (°)	ω	280.70934(12)	280.68643(12)
Longitude of ascending node (°)	Ω	347.1826006(47)	347.1801977(47)
Time of periapsis (TDB)[a]	t_p	2023 Nov 16.4216(28)	2023 Nov 16.7039(28)
Epoch (TDB)[a]		1709 May 20.6 ± 1.6	2338 Sep 20.1 ± 1.6

Notes. Both of the original and future orbits are in reference to the Solar System barycenter in the J2000 ecliptic coordinate system at epochs when each of the clones is at pre- and postperihelion heliocentric distances 250 au, respectively. The uncertainties of the orbital elements are standard deviations computed from distributions of the 5001 clones.
[a] The uncertainties are in days.

Appendix B). Because our focus was on secular variation in the orbit, following Heisler & Tremaine (1986), we averaged the Hamiltonian in Equation (8) over the orbital period, thereby obtaining the orbit-averaged disturbing function:

$$\bar{\mathcal{R}} = -\pi G \rho_* a^2 (1 - e^2 + 5e^2 \sin^2 \tilde{\omega}) \sin^2 \tilde{\imath}. \quad (9)$$

Given the relation between the periapsis distance q, the semimajor axis a, and the eccentricity e of the orbit, namely, $q = a(1 - e)$, we can write the time derivative of the periapsis distance as

$$\dot{q} = (1 - e)\dot{a} - a\dot{e}, \quad (10)$$

in which $\dot{a}$ and $\dot{e}$ can be computed by applying Lagrange's planetary equations (e.g., Roy 2005):

$$\dot{a} = \left(\frac{2}{na}\right)\frac{\partial\bar{\mathcal{R}}}{\partial\chi}, \tag{11}$$

$$\dot{e} = \frac{1}{na^2 e}\left[(1 - e^2)\frac{\partial\bar{\mathcal{R}}}{\partial\chi} - \sqrt{1 - e^2}\frac{\partial\bar{\mathcal{R}}}{\partial\tilde{\omega}}\right]. \tag{12}$$

Here, n is the mean motion and $\chi = -nt_p$, in which t_p is the time of periapsis passage. Substituting with Equation (9), we can derive

$$\dot{a} = 0, \tag{13}$$

$$\dot{e} = 5\pi G\rho_*\frac{e\sqrt{1 - e^2}}{n}\sin^2\tilde{\iota}\sin 2\tilde{\omega}. \tag{14}$$

The first equation reveals that the semimajor axis of the orbit is a constant, as long as the perturbation is solely from the Galactic tide. Assuming there is no significant change in $\tilde{\iota}$ and $\tilde{\omega}$ with time, we can then apply the method of separation of variables to integrate the second equation, yielding

$$\text{sech}^{-1}e_o - \text{sech}^{-1}e \approx 5\pi G\rho_*\frac{\Delta t}{n}\sin^2\tilde{\iota}\sin 2\tilde{\omega} \tag{15}$$

in a time interval from t_o to $t_o + \Delta t$. The eccentricity at initial time is denoted with the subscript "o." Setting $|\Delta t| = 2\pi/n$, i.e., the orbital period of the comet, we can find the secular change in the periapsis distance between two successive returns of the comet due to the Galactic tide to be

$$\Delta q = q - q_0$$
$$\approx a\left[e_o - \text{sech}\left(\text{sech}^{-1}e_o \pm 10\pi^2\frac{G\rho_*}{\mu_0}a^3\sin^2\tilde{\iota}\sin 2\tilde{\omega}\right)\right]. \tag{16}$$

Here, the mean motion has been substituted with the relation $\mu_0 = n^2 a^3$, the plus sign is taken if the integration in Equation (15) is backward in time, and the minus sign is taken otherwise. Via substitution with the obtained values of pertinent orbital elements of the original barycentric orbit referenced to the Galactic plane, we attained the periapsis distance of the previous return of the comet to be 87 ± 5 au. Therefore, our analytical result strongly favors the conclusion that C/2019 E3 is a dynamically new comet from the Oort spike. In other words, the current return of the comet is most likely its first ever passage into the planetary region since it was ejected to the outer edge of the Solar System. Given its long orbital period ($\sim$6.6 Myr), it is highly unlikely that the observed activity of the comet would be caused by retained heat from the previous return.

In a similar fashion, we investigated the next return of the comet by integrating the 5001 clones forward in time until they reached a postperihelion heliocentric distance of $r_H = 250$ au, using exactly the same force model in mercury6. We append the statistics of the orbital elements of the "future" orbit to Table 4, from which we can notice that, if the comet survives the forthcoming perihelion passage, its orbital energy will decrease as a consequence of planetary perturbations. The change in the orbital energy is within the expected range of other large-perihelion comets from the Oort spike

(Królikowska & Dybczyński 2017). In the same manner, yet with the Keplerian orbital elements of the future barycentric orbit, we found the change in the periapsis distance between the current and next returns to be $\Delta q = -3.18 \pm 0.06$ au, corresponding to an even smaller periapsis distance of 7.13 ± 0.06 au for the next return of the comet.

To check the reliability of our results from the analytical approach, we still employed mercury6 and integrated the nominal orbit of the comet (Table 3) both backward and forward in time until the previous and future returns were reached. We reduced the list of massive bodies to the eight major planets, Pluto, and the three most massive asteroids, so as to reduce the computational cost as much as possible. We assumed the linear theory for uncertainty propagation, whereby the error in the periapsis distance can be evaluated from

$$\sigma_q \approx \left[\left(\frac{\partial q}{\partial\boldsymbol{E}_o}\right)\boldsymbol{C}_o\left(\frac{\partial q}{\partial\boldsymbol{E}_o}\right)^\top\right]^{1/2}. \tag{17}$$

Here, $\boldsymbol{E}_o$ and $\boldsymbol{C}_o$ respectively are the Keplerian orbital elements and the corresponding covariance matrix at initial time. We computed the partial derivatives using finite differences numerically in mercury6, thus finding the previous and future periapsis distances of the comet to be $q = 71 \pm 4$ au and 7.61 ± 0.06 au, respectively. The result for the previous return is in reasonable agreement with the counterpart from the analytical approach at the 2σ level, given the approximations in the analytical approach. Yet the difference between the results for the next perihelion is at the 5σ level. Such a worse discrepancy is not surprising whatsoever, in that the comet will not only be perturbed by the Galactic tide, but also more profoundly by the major planets when it is well within the planetary region, which we completely ignored in the analytical approach. Despite these issues, the predicted trends for the periapsis distance of the comet, which is expected to further decrease in the next return, are consistent in both approaches. However, we could not determine whether the comet will stay within or be ejected from the Solar System after its next return in $\sim$2.3 Myr, because of the current orbital uncertainty.

We are fully aware of two major drawbacks in our analysis for the orbital evolution, namely that nongravitational effects and gravitational perturbations from nearby passing stars were not taken into account. To address the former, we still utilized Find_Orb, yet assumed a nongravitational acceleration stemming from sublimation of supervolatiles scaled as r_H^{-2}, and included the radial, transverse, and normal nongravitational parameters defined by Marsden et al. (1973) as additional free parameters to fit the astrometric observations of the comet. The result was that including the nongravitational parameters brought forth no clear improvement in the astrometric residuals of the solution, and that values of the best-fit nongravitational parameters are all statistically consistent with zero (signal-to-noise ratios <1). We therefore conclude that nongravitational effects of C/2019 E3 are negligible.

Now we proceed to discuss the second drawback. Using the Gaia DR2 catalog and accounting for incompleteness, Bailer-Jones et al. (2018) inferred a nontrivial stellar encounter rate within 1 pc of the present-day Solar System to be $\sim$20 $\pm$ 2 Myr^{-1}. Indeed, as an example, strong perturbations on the orbital evolution of C/2014 UN$_{271}$ by stellar encounters were reported in Dybczyński & Królikowska (2022). On the other

hand, Królikowska & Dybczyński (2017) identified no stellar encounter sufficient to alter the dynamical status of the analyzed comets. Given these factors, we are inclined to believe that our conclusion about C/2019 E3 being a dynamically new comet likely remains valid, despite neglecting stellar perturbations. However, we do suggest that our estimates of the previous and next periapsis distances should be better regarded as preliminary results, which need to be robustly verified by means of N-body integration accounting perturbations from passing stars. That verification is beyond the scope of this work. We noticed a fairly recent update of the Catalogue of Cometary Orbits and their Dynamical Evolution[9] (CODE) by Królikowska & Dybczyński (2020, 2023) that 29 comets discovered between 2019 and early 2021, including C/2019 E3, were newly added to the database. Although their orbit determination for C/2019 E3 was based on available astrometric observations of a shorter arc spanning from 2015 January to 2023 May, they also arrived at the same conclusion as ours, i.e., that C/2019 is a dynamically new comet, with a previous periapsis distance of $q = 60 \pm 5$ au in the model where only the Galactic tide was included, and 441 ± 6 au in the model where stellar perturbations were also taken into account. Unfortunately, the future orbital evolution of the comet is not available from the CODE catalog. Nevertheless, the dynamical status of C/2019 E3 being a dynamically new comet appears to be conclusive.

4.4. Comparison of the Known Ultradistant Comets

Here, we compare ultradistant comets that exhibited preperihelion cometary activity at heliocentric distances $r_H \gtrsim 20$ au. Noteworthily, it came to our attention that Królikowska & Dones (2023) included three astrometric measurements of comet C/2006 S3 (LONEOS) at a preperihelion heliocentric distance of $r_H = 26.1$ au, all from 1999 October 13, in their orbit determination, implying the comet to be an additional ultradistant comet. On the other hand, these astrometric measurements were found to be outliers with large residuals that could not fit any of the orbital solutions for the comet by these authors. After querying astrometry for the comet in the Minor Planet Center Database Search, we found that the three astrometric measurements no longer existed. Moreover, the earliest astrometry of the comet used in orbit determination by the Minor Planet Center and JPL Horizons was no earlier than 2006 August, when the comet was at ~14 au from the Sun. As such, we suspect that the single-night observation of the comet from 1999 is erroneous, and we do not count C/2006 S3 as a known ultradistant comet. It is also worth noting that comet C/1995 O1 (Hale–Bopp) was observed to exhibit activity at great heliocentric distances $\gtrsim 20$ au as well (Szabó et al. 2008; Kramer et al. 2014). However, the observed activity at $r_H \gtrsim 20$ au was all postperihelion, and there is no reported observation showing its activity at similarly great heliocentric distances preperihelion. Thus, it is not counted here either. As a result, there are four known samples of ultradistant comets to date: C/2010 U3, C/2014 UN$_{271}$, C/2017 K2, and C/2019 E3.

First of all, let us compare the original orbits of the four ultradistant comets. For C/2010 U3, C/2014 UN$_{271}$, and C/2017 K2, we simply adopt the "preferred" solutions from the CODE catalog. We show the comparison together with other

long-period comets from the CODE catalog in multidimensional space of the orbital elements in Figure 8, where we can find no obvious trend in the orbital distribution, except that they all have considerable orbital inclinations with respect to the ecliptic. In terms of original orbits, the known ultradistant comets are not distinguishable from other long-period comets.

Now we discuss the dynamical statuses of the known ultradistant comets. According to the CODE catalog, C/2010 U3 is confidently labeled as a dynamically new comet, whereas C/2017 K2 was formerly reported to be "almost certainly" a dynamically old comet by Królikowska & Dybczyński (2018). However, even though the observing arc of the comet was extended, its dynamical status turned out to be far more equivocal than previously expected, primarily owing to great uncertainties in a potential close encounter with a nearby passing star (Dybczyński & Królikowska 2022). As for C/2014 UN$_{271}$, Bernardinelli et al. (2021) concluded the comet to be dynamically new, which is largely supported by Dybczyński & Królikowska (2022), with the exception that the latter authors also identified a nontrivial number of cases where the comet entered the planetary region in the previous perihelion return. Together with the results for C/2019 E3 (Section 4.3), there seems to be a fair chance that all four of the known ultradistant comets are dynamically new. Yet this remains to be affirmed by force models with more precise kinematics of both the comets and nearby passing stars.

Next, we compare the physical properties of the four ultradistant comets. Their general surface brightness profiles were all measured to be consistent with steady-state behaviors, suggestive of prolonged sublimation of supervolatiles (Jewitt et al. 2017; Hui et al. 2019; Jewitt et al. 2019; Hui et al. 2022; Kelley et al. 2022). Morphologically, C/2019 E3 and C/2017 K2 highly resembled each other, as no obvious tail was visible at heliocentric distances $r_H \gtrsim 10$ au, implying the optical dominance of large-sized (submillimeter-scaled or greater) dust particles ejected at speeds no greater than a few meters per second. Conversely, at similar distances from the Sun, C/2010 U3 and C/2014 UN$_{271}$ showed obvious tails. In particular, in the case of C/2010 U3, the Monte Carlo dust modeling by Hui et al. (2019) suggested that the coma and tail of the comet consisted of much smaller dust grains of ~10 μm ejected at speeds of $\lesssim 50$ m s^{-1} and subjected to the Lorentz force in addition to the solar gravitation and radiation pressure. For C/2014 UN$_{271}$, we are unaware of any Monte Carlo dust modeling in the published literature. Yet the syndyne analysis by Farnham et al. (2021) suggests that the observed dust coma and tail are comprised of dust grains of submillimeter scale ejected in the sunward hemisphere of the nucleus at faster speeds of ~10 m s^{-1}. Thus, although the known ultradistant comets were likely all driven by sublimation of supervolatiles in a steady state, there may exist a diversity in the physical properties of their dust environments. Nevertheless, the discoveries of ultradistant comets still act as a serious challenge to the classical activity model for comets, which predicts no cometary activity whatsoever at heliocentric distances $\gtrsim 10$ au, due to interparticle cohesion being overlarge for the drag force from outgassing supervolatiles to overcome (Gundlach et al. 2015; Jewitt et al. 2019). Recent promising resolutions of the dilemma include accounting for gas diffusion inside the pebbles of which a cometary nucleus is comprised (Fulle et al. 2020) and sublimation through a porous mantle (Bouziani

---
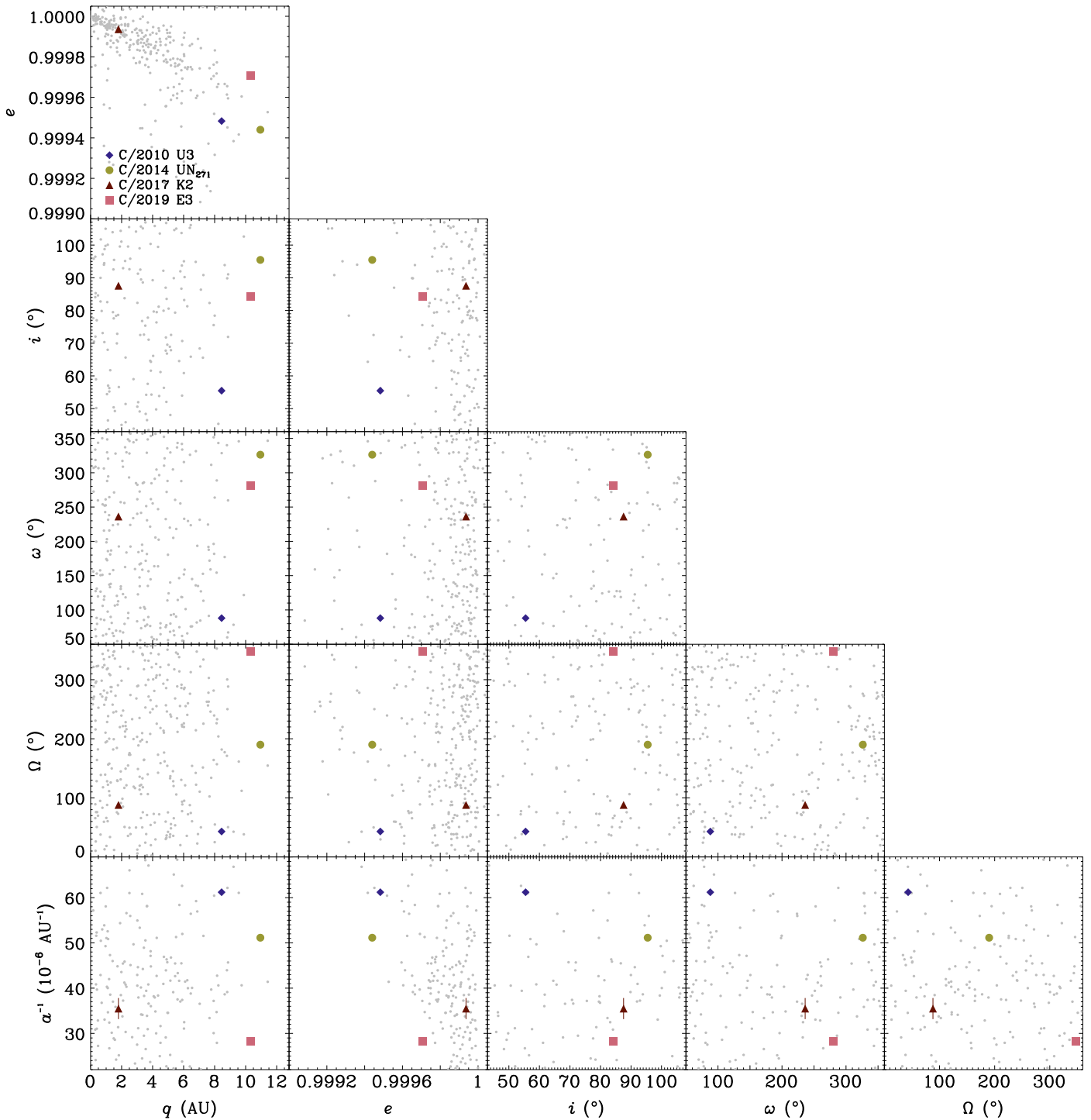
Figure 8. Comparison between periapsis distance (q), eccentricity (e), inclination (i), argument of periapsis (ω), longitude of ascending node (Ω), and reciprocal of the semimajor axis (a^{-1}) of original Solar System barycentric J2000 ecliptic orbits of the four known ultradistant comets C/2010 U3, C/2014 UN$_{271}$, C/2017 K2, and C/2019 E3 (color coded by bold symbols; see the legend in the upper left). Background dots in gray are other long-period comets, whose original orbits together with those of the three previously known ultradistant comets are based on the preferred solutions in the CODE catalog. Associated 1σ formal errors in the orbital elements of the ultradistant comets are also included in the plots. However, as they are in general much smaller than the displayed ranges here, they are basically invisible, except for C/2017 K2 in terms of its reciprocal of the semimajor axis.

& Jewitt 2022), but they remain to be further verified with more observations of ultradistant comets.

Before concluding this section, we also compare the activity of the four ultradistant comets. At heliocentric distances $\gtrsim$20 au, the apparent magnitudes of these comets were not greatly different from each other, with C/2014 UN$_{271}$ being somewhat brighter, presumably at least in part attributable to its

exceptionally enormous nucleus size (Hui et al. 2022; Lellouch et al. 2022). However, as these comets neared the Sun, there seem to be two primary types to which the four ultradistant comets belong. The first type includes C/2017 K2 and C/2019 E3, whose activity in general monotonically increased in highly similar manners without observational evidence of outbursts. The other type contains C/2010 U3 and C/2014 UN$_{271}$, which

exhibited clear outbursts in brightness (Hui et al. 2019; Kelley et al. 2022). While we cannot completely rule out the possibility of outbursts of C/2017 K2 and C/2019 E3 evading the available observations, it still seems reasonable to conclude that outbursts at comets of the first type occurred on a rarer basis as compared to the counterparts of the other type.

At the current stage, as we are only beginning to discover ultradistant comets and there are only four known samples, we have little practical knowledge about this population itself and very few clues about how they can be active even at great distances from the Sun. In order to acquire a better understanding of these comets, observations of far more members of this population are desired. With the advent of state-of-the-art all-sky surveys such as the Legacy Survey of Space and Time program to be conducted starting from 2025 at the Vera C. Rubin Observatory (Ivezić et al. 2019), it is suggested that hundreds to thousands of long-period comets with perihelion distances $\gtrsim 5$ au will be discovered in the near future (Silsbee & Tremaine 2016). These new observations would allow for an advancement in our understanding of the ultradistant comet population and their activity.

5. Summary

In this paper, we presented analyses of serendipitous archival observations of comet C/2019 E3. Key findings of our study include:

1. We identified C/2019 E3 (ATLAS) as the fourth known ultradistant comet that displayed prolonged activity at heliocentric distances $r_H \gtrsim 20$ au preperihelion, after C/2010 U3 (Boattini), C/2014 UN$_{271}$ (Bernardinelli–Bernstein), and C/2017 K2 (PANSTARRS).

2. The measurements of the surface brightness profile of the comet reveal that the activity was consistent with steady-state scenarios, thus suggesting the mass loss was driven by sublimation of supervolatiles (e.g., CO and CO_2), given the great heliocentric distances of the comet. The effective scattering cross section of dust increased steadily as the comet approached the Sun, varying with heliocentric distance as $r_H^{-1.5 \pm 0.4}$ over the monitored course from 2012 to 2019. We estimated a total and a net mass-loss rate of dust of $\gtrsim 10^2$ and $\gtrsim 10\,\mathrm{kg\,s^{-1}}$, respectively, for the comet.

3. Our photometry of the comet indicates its color was similar to those of other long-period comets, except in $g - r$, which was measured to be slightly bluer. Based on our photometry, assuming a geometric albedo of $p_r = 0.05$, and adopting several empirical thermophysical models for sublimation of CO and CO_2, we constrained the nucleus of the comet to be greater than ~ 3 km in diameter.

4. The apparent morphology of the comet basically remained circularly symmetric without an obvious tail. Results from our Monte Carlo dust modeling suggest that the observed dust environment of the comet was most likely optically dominated by mm-scaled dust grains ejected from the sunlit hemisphere of the nucleus at speeds $\lesssim 0.4\,\mathrm{m\,s^{-1}}$.

5. We performed an improved orbit determination for the comet with our astrometry, based upon which we analytically derived that the comet is likely dynamically new and that its periapsis distance will further shrink in the next return, due to the Galactic tide, assuming the comet will physically survive. Although the detailed values of the periapsis distances in the previous and next returns are preliminary and should be verified by a more sophisticated dynamical model where perturbations from stellar encounters are taken into account, the dynamical status of C/2019 E3 being a dynamically new comet is incontestable.

6. Our comparison of the four known ultradistant comets reveals no obvious trend seen in their orbital elements. Nor do they exhibit outstanding orbital traits if compared to other long-period comets. While there possibly exists a diversity in the physical properties of their dust environments, there seem to be two types into which these comets can be grouped: (1) C/2017 K2 and C/2019 E3 increased their activity in a basically monotonic manner as they approached the Sun, and (2) C/2010 U3 and C/2014 UN$_{271}$ exhibited obvious outbursts in brightness at similar heliocentric distances. We need more data on this distant comet population before we can achieve a better understanding of them and their activity.

Facility: Blanco (DECam), PO: 1.2m (ZTF), PS1, Sky-Mapper, VST (OmegaCAM).

Software: Find_Orb, IDL, mercury6 (Chambers 1999).

Appendix A
Equation of Motion Perturbed by Galactic Tide

Adopting the Galactic tide model by Heisler & Tremaine (1986), Fouchard et al. (2005) presented the equations of motion of a comet perturbed by the Galactic tide in a mixture of fixed and rotating Cartesian Galactic coordinates. Starting with their results, we express the equation of motion of the comet in the J2000 barycentric Cartesian Galactic coordinates $(x, y, z)^\top$

in a matrix form as

$$\begin{pmatrix} \ddot{x} \\ \ddot{y} \\ \ddot{z} \end{pmatrix} = -\frac{\mu_0}{r^3}\begin{pmatrix} x \\ y \\ z \end{pmatrix} - \begin{pmatrix} \mathcal{G}_1\cos 2\Omega_\odot t & \mathcal{G}_1\sin 2\Omega_\odot t & 0 \\ \mathcal{G}_1\sin 2\Omega_\odot t & -\mathcal{G}_1\cos 2\Omega_\odot t & 0 \\ 0 & 0 & \mathcal{G}_3 \end{pmatrix}\begin{pmatrix} x \\ y \\ z \end{pmatrix}, \tag{A1}$$

where $r = \sqrt{x^2 + y^2 + z^2}$ is the barycentric distance of the comet, $\Omega_\odot = -26$ km s^{-1} kpc^{-1} is the angular speed of the Sun around the Galactic center, $\mathcal{G}_1 = -\Omega_\odot^2$ and $\mathcal{G}_3 = 4\pi G\rho_*$ are the Oort constants, and t is time from J2000. The first and second terms on the right-hand side of Equation (A1) correspond to the contribution from the gravity of the Solar System barycenter and that from the Galactic tide, respectively.

Let $\boldsymbol{R}$ denote the 3×3 transformation matrix from the ecliptic reference frame $(X, Y, Z)^\top$ to the Galactic one $(x, y, z)^\top$ at epoch J2000, when the obliquity of the ecliptic is $\epsilon = 23°26'21''.448$, the R.A. and decl. coordinates of the north Galactic pole are $\alpha_G = 192°.85948$ and $\delta_G = +27°.12825$, respectively, and the Galactic longitude of the ascending node of the Galactic plane on the celestial equator is $l_\Omega = 32°.93192$ (ESA 1997). As such, the transformation from the ecliptic reference frame to the Galactic one can be achieved by rotating first about the first axis by ϵ clockwise, then counterclockwise around the third axis by $\pi/2 + \alpha_G$, followed by counterclockwise around the first axis by $\pi/2 - \delta_G$, and finally clockwise about the third axis by l_Ω, i.e.,

$$\boldsymbol{R} = \boldsymbol{R}_3(-l_\Omega)\boldsymbol{R}_1\left(\frac{\pi}{2} - \delta_G\right)\boldsymbol{R}_3\left(\frac{\pi}{2} + \alpha_G\right)\boldsymbol{R}_1(-\epsilon). \tag{A2}$$

Here, $\boldsymbol{R}_j(\theta)$ ($j = 1, 2, 3$) represents the 3×3 rotation matrix that performs a rotation about the ith axis of the coordinate system by an angle of θ (>0 for counterclockwise rotation, otherwise clockwise) in $\mathbb{R}^3$. Our result for the transformation matrix to ten decimal digits is

$$\boldsymbol{R} = \begin{pmatrix} -0.0548755604 & -0.9938213791 & -0.0964766261 \\ +0.4941094279 & -0.1109907334 & +0.8622858751 \\ -0.8676661490 & -0.0003515899 & +0.4971471917 \end{pmatrix}. \tag{A3}$$

Thereby, the acceleration of the comet due to the Galactic tide in the Cartesian ecliptic coordinates at J2000 can be easily obtained from the second term on the right-hand side of Equation (A1) with the transformation matrix as

$$\begin{pmatrix} \ddot{X} \\ \ddot{Y} \\ \ddot{Z} \end{pmatrix}_{\text{tide}} = -\boldsymbol{R}^\top\begin{pmatrix} \mathcal{G}_1\cos 2\Omega_\odot t & \mathcal{G}_1\sin 2\Omega_\odot t & 0 \\ \mathcal{G}_1\sin 2\Omega_\odot t & -\mathcal{G}_1\cos 2\Omega_\odot t & 0 \\ 0 & 0 & \mathcal{G}_3 \end{pmatrix}\boldsymbol{R}\begin{pmatrix} X \\ Y \\ Z \end{pmatrix}, \tag{A4}$$

which we implemented and added to the subroutine mfo_user() in mercury6.

Appendix B
Conversions between Ecliptic and Galactic Orbital Elements

The transformation between the Galactic and ecliptic reference frames is purely rotational and therefore lengths are conserved; the only influenced Keplerian orbital elements are the inclination i, longitude of ascending node Ω, and argument of periapsis ω. In the following, we present the conversions from the ecliptic reference frame to the Galactic one for the

three aforementioned Keplerian orbital elements:

$$\cos \tilde{\imath} = (R_{31} \sin \Omega - R_{32} \cos \Omega) \sin i + R_{33} \cos i, \quad \text{(B1)}$$

$$\sin \tilde{\Omega} = \frac{(R_{11} \sin \Omega - R_{12} \cos \Omega) \sin i + R_{13} \cos i}{\sin \tilde{\imath}}, \quad \text{(B2)}$$

$$\cos \tilde{\Omega} = -\frac{(R_{21} \sin \Omega - R_{22} \cos \Omega) \sin i + R_{23} \cos i}{\sin \tilde{\imath}}, \quad \text{(B3)}$$

$$\sin \tilde{\omega}' = \frac{(R_{31} \cos \Omega + R_{32} \sin \Omega) \cos \omega' - [(R_{31} \sin \Omega - R_{32} \cos \Omega) \cos i - R_{33} \sin i] \sin \omega'}{\sin \tilde{\imath}}, \quad \text{(B4)}$$

$$\cos \tilde{\omega}' = \frac{R_{11}[R_{22} \sin i \cos \omega' + R_{23}(\sin \Omega \sin \omega' - \cos i \cos \Omega \cos \omega')]}{\sin \tilde{\imath}}$$
$$- \frac{R_{12}[R_{21} \sin i \cos \omega' + R_{23}(\cos \Omega \sin \omega' + \cos i \sin \Omega \cos \omega')]}{\sin \tilde{\imath}}$$
$$- \frac{R_{13}[R_{21}(\sin \Omega \sin \omega' - \cos i \cos \Omega \cos \omega') - R_{22}(\cos \Omega \sin \omega' + \cos i \sin \Omega \cos \omega')]}{\sin \tilde{\imath}}. \quad \text{(B5)}$$

In the above equations, R_{kl} denotes the element in the kth row and lth column of transformation matrix $\boldsymbol{R}$, and the symbol $\tilde{\square}$ denotes the corresponding Keplerian orbital elements in the Galactic reference frame, $\square' = \square + f$, where f is the true anomaly, a quantity calculable from the mean anomaly and independent from the selection of the reference system.

The conversions from the Galactic reference frame to the ecliptic one for the three Keplerian orbital elements can be conveniently obtained by simply swapping the Galactic and ecliptic orbital elements as well as the indices of rows and columns in Equations (B1)–(B5), thanks to the property of $\boldsymbol{R}^{-1} = \boldsymbol{R}^{\top}$.

ORCID iDs

Man-To Hui (許文韜) ⓘ https://orcid.org/0000-0001-9067-7477
Robert Weryk ⓘ https://orcid.org/0000-0002-0439-9341
Marco Micheli ⓘ https://orcid.org/0000-0001-7895-8209
Richard Wainscoat ⓘ https://orcid.org/0000-0002-1341-0952

References

A'Hearn, M. F., Feaga, L. M., Keller, H. U., et al. 2012, ApJ, 758, 29
Agarwal, J., Kim, Y., Kelley, M. S. P., et al. 2023, arXiv:2309.12759
Bailer-Jones, C. A. L., Rybizki, J., Andrae, R., et al. 2018, A&A, 616, A37
Bellm, E. C., Kulkarni, S. R., Graham, M. J., et al. 2019, PASP, 131, 018002
Bernardinelli, P. H., Bernstein, G. M., Montet, B. T., et al. 2021, ApJL, 921, L37
Bouziani, N., & Jewitt, D. 2022, ApJ, 924, 37
Chambers, J. E. 1999, MNRAS, 304, 793
Chambers, K. C., Magnier, E. A., Metcalfe, N., et al. 2016, arXiv:1612.05560
Dybczyński, P. A. 2001, A&A, 375, 643
Dybczyński, P. A., & Królikowska, M. 2022, A&A, 660, A100
Eggl, S., Farnocchia, D., Chamberlin, A. B., et al. 2020, Icar, 339, 113596
ESA 1997, ESA SP-1200, The Hipparcos and Tycho Catalogues (Noordwijk: ESA)
Farnham, T. L., Kelley, M. S. P., & Bauer, J. M. 2021, PSJ, 2, 236
Flaugher, B., Diehl, H. T., Honscheid, K., et al. 2015, AJ, 150, 150
Fouchard, M., Froeschlé, C., Matese, J. J., et al. 2005, CeMDA, 93, 229
Fray, N., & Schmitt, B. 2009, P&SS, 57, 2053
Fulle, M. 2004, in Comets II, ed. M. C. Festou, H. U. Keller, & H. A. Weaver (Tucson, AZ: Univ. Arizona Press), 565
Fulle, M., Blum, J., & Rotundi, A. 2020, A&A, 636, L3
Gaia Collaboration, Brown, A. G. A., Vallenari, A., et al. 2018, A&A, 616, A1
Gaia Collaboration, Vallenari, A., Brown, A. G. A., et al. 2023, A&A, 674, A1
Graham, M. J., Kulkarni, S. R., Bellm, E. C., et al. 2019, PASP, 131, 078001
Gronoff, G., Maggiolo, R., Cessateur, G., et al. 2020, ApJ, 890, 89
Guilbert-Lepoutre, A. 2012, AJ, 144, 97
Gundlach, B., Blum, J., Keller, H. U., et al. 2015, A&A, 583, A12
Gwyn, S. D. J., Hill, N., & Kavelaars, J. J. 2012, PASP, 124, 579

Harrington Pinto, O., Womack, M., Fernandez, Y., et al. 2022, PSJ, 3, 247
Heisler, J., & Tremaine, S. 1986, Icar, 65, 13
Hui, M.-T., Farnocchia, D., & Micheli, M. 2019, AJ, 157, 162
Hui, M.-T., Jewitt, D., & Clark, D. 2018, AJ, 155, 25
Hui, M.-T., Jewitt, D., Yu, L.-L., et al. 2022, ApJL, 929, L12
Ishiguro, M. 2008, Icar, 193, 96
Jewitt, D., Agarwal, J., Hui, M.-T., et al. 2019, AJ, 157, 65
Jewitt, D., Hui, M.-T., Mutchler, M., et al. 2017, ApJL, 847, L19
Jewitt, D., Kim, Y., Mutchler, M., et al. 2021, AJ, 161, 188
Ivezić, Ž., Kahn, S. M., Tyson, J. A., et al. 2019, ApJ, 873, 111
Keller, S. C., Schmidt, B. P., Bessell, M. S., et al. 2007, PASA, 24, 1
Kelley, M. S. P., Kokotanekova, R., Holt, C. E., et al. 2022, ApJL, 933, L44
Kelley, M. S. P., Woodward, C. E., Gehrz, R. D., et al. 2017, Icar, 284, 344
Knight, M. M., Kokotanekova, R., & Samarasinha, N. H. 2023, arXiv:2304.09309
Kramer, E. A., Fernandez, Y. R., Lisse, C. M., et al. 2014, Icar, 236, 136
Królikowska, M., & Dones, L. 2023, A&A, 678, A113
Królikowska, M., & Dybczyński, P. A. 2017, MNRAS, 472, 4634
Królikowska, M., & Dybczyński, P. A. 2018, A&A, 615, A170
Królikowska, M., & Dybczyński, P. A. 2020, A&A, 640, A97
Królikowska, M., & Dybczyński, P. A. 2023, arXiv:2311.04063
Kuijken, K., Bender, R., Cappellaro, E., et al. 2002, Msngr, 110, 15
Lellouch, E., Moreno, R., Bockelée-Morvan, D., et al. 2022, A&A, 659, L1
Levasseur-Regourd, A.-C., Agarwal, J., Cottin, H., et al. 2018, SSRv, 214, 64
Maggiolo, R., Gronoff, G., Cessateur, G., et al. 2020, ApJ, 901, 136
Marsden, B. G., Sekanina, Z., & Yeomans, D. K. 1973, AJ, 78, 211
Masci, F. J., Laher, R. R., Rusholme, B., et al. 2019, PASP, 131, 018003
Meech, K. J., & Jewitt, D. C. 1987, A&A, 187, 585
Meech, K. J., Kleyna, J. T., Hainaut, O., et al. 2017, ApJL, 849, L8
Park, R. S., Folkner, W. M., Williams, J. G., et al. 2021, AJ, 161, 105
Roy, A. E. 2005, in Orbital Motion, ed. A. E. Roy (4th ed.; Bristol: IOP Publishing), 526
Schambeau, C. A., Fernández, Y. R., Lisse, C. M., et al. 2015, Icar, 260, 60
Schambeau, C. A., Fernández, Y. R., Samarasinha, N. H., et al. 2021, PSJ, 2, 126
Silsbee, K., & Tremaine, S. 2016, AJ, 152, 103
Solontoi, M., Ivezić, Ž., Jurić, M., et al. 2012, Icar, 218, 571
Szabó, G. M., Kiss, L. L., Pál, A., et al. 2012, ApJ, 761, 8
Szabó, G. M., Kiss, L. L., & Sárneczky, K. 2008, ApJL, 677, L121
Tonry, J. L., Denneau, L., Flewelling, H., et al. 2018, ApJ, 867, 105
Tonry, J. L., Stubbs, C. W., Lykke, K. R., et al. 2012, ApJ, 750, 99
Vereš, P., Farnocchia, D., Chesley, S. R., et al. 2017, Icar, 296, 139
Waters, C. Z., Magnier, E. A., Price, P. A., et al. 2020, ApJS, 251, 4
Willmer, C. N. A. 2018, ApJS, 236, 47
Womack, M., Sarid, G., & Wierzchos, K. 2017, PASP, 129, 031001
Young, D., Kilmartin, P., Lister, T., et al. 2019, MPEC, 2019, F54